Ultrasonic Imaging Using a Computed Point Spread Function

Ramsharan Rangarajan, C. V. Krishnamurthy, and Krishnan Balasubramaniam

Abstract—An explicit point spread function (PSF) evaluator in the frequency domain is described for an ultrasonic transducer operating in the pulse-echo mode. The PSF evaluator employs the patch element model for transducer field determination and scattered field assessment from a small but finite "point" reflector. The PSF for a planar transducer in a medium has been evaluated in the near and the far field. The computed PSFs were used to deconvolve and restore surface images, obtained experimentally, of a single hole and a five-hole cluster in an Al calibration block. A calibration plot is arrived at for estimating, without the need for deconvolution, the actual diameters of circular reflectors from apparent diameters obtained experimentally for a single-medium imaging configuration. The PSF, when the transducer and the point reflector are in two media separated by a planar interface, was evaluated in the near and far field. The computed PSFs were used to deconvolve and restore subsurface images, obtained experimentally, of flat bottom holes (FBHs) in an Al calibration block. We show that the PSF, in the presence of a planar interface, can be obtained from a single-medium PSF model using an effective single-medium path length concept. The PSFs and modulation transfer functions (MTFs) are evaluated for spherical focused and annular transducers and compared with those for the planar transducer. We identify imaging distances to get better-resolved images when using planar, spherical focused, and annular transducers.

I. INTRODUCTION

ULTRASONIC imaging is an important aspect of nondestructive evaluation of industrial components capable of providing qualitative as well as quantitative information. Industrial imaging tools are being constantly improved at both the hardware and the software levels to achieve better quality images and higher resolution [1]. While it is known that image degradation is due to the radiation and reception characteristics of the sensors, much of the effort has been directed toward developing "blind" deconvolution techniques without involving explicit sensor characteristics [2], [3]. These techniques are general but applicable only in the far field, and do not exploit sensor characteristics fully. Efforts to obtain higher resolution

R. Rangarajan is with the Department of Mechanical Engineering, Stanford University, Stanford, CA 94305 (e-mail: r.ramsharan@gmail.com).

C. V. Krishnamurthy is with the Centre for Nondestructive Evaluation, Department of Mechanical Engineering, Indian Institute of Technology Madras, Chennai, Tamilnadu, 600036 India.

K. Balasubramaniam is with the Department of Mechanical Engineering, Indian Institute of Technology Madras, Chennai, Tamilnadu 600036 India.

images using newer transducer designs or newer configurations also need to exploit sensor characteristics explicitly to succeed.

Ultrasonic transducers are commonly used in pulse-echo mode to generate C-scans of components, and the resolution criterion in the far field is distinct from Rayleigh's criterion applicable for the receive-only mode. Another common feature in the generation of C-scan images is the presence of an interface between the medium being inspected and the fluid in which the medium is immersed. The influence on the resolution and image quality due to the interface position with respect to the transducer on the one side and the flaw(s) on the other side needs to be understood.

C-scans carry volume information since they record data from every depth in the specimen. To image the plane of interest, C-scans have to be gated in time so that information specific to only that plane is recorded. Broadband transducers are preferred as they offer reasonably short duration pulses leading to good axial resolution. The time-gated signal has different frequency components in the Fourier domain, determined by the bandwidth of the imaging system. The ultrasonic image in the frequency domain is obtained by monitoring a specific frequency component (usually the center frequency of the transducer) of this time-gated signal. However, this image is never an exact representation of the object since the image creation and reconstruction are both influenced by the imaging distance, the scan step, and the transducer beam divergence (governed by its shape, size, and frequency).

The two-dimensional (2-D) point spread function (PSF) characterizes the image degradation caused by the transducer and helps determine its lateral resolution capabilities [4]. The advantage of deconvolving with a pulse-echo mode PSF taking into account certain transducer characteristics as well as the interface effects has been demonstrated [5]. The PSF of an imaging system in the pulse-echo mode is the image of a point reflector as insonified and recorded by it. Since any reflecting plane surface being imaged can be thought of as a collection of point reflectors, the image $g(x, y)$ is formed by a convolution of the object $f(x, y)$ and the system PSF $h(x, y)$, i.e.,

$$g(x, y) = h(x, y) \otimes f(x, y), \qquad (1)$$

where $\otimes$ denotes the convolution operator.

The Fourier transform of the object $F(u, v)$ can be recovered by a direct division in the spatial frequency domain (u, v) as

$$F(u,v) = \frac{G(u,v)}{H(u,v)}, \qquad (2)$$

where $G(u,v)$ and $H(u,v)$ are the Fourier transforms of g and h. The object f can then be obtained by an inverse Fourier transform of F. However, there is always some degradation of the image $g(x,y)$ due to noise, $n(x,y)$ in the recording system. Thus,

$$g(x,y) = h(x,y) \otimes f(x,y) + n(x,y). \qquad (3)$$

The restoration procedure now has to be written as

$$F(u,v) = \frac{G(u,v)}{H(u,v)} - \frac{N(u,v)}{H(u,v)}, \qquad (4)$$

with $N(u,v)$ being the Fourier transform of $n(x,y)$. In these equations, it is tacitly assumed that there is no degradation of the PSF due to noise. However, an experimentally measured PSF (i.e., a C-scan image of a "point" reflector, usually a small steel ball, with the same parameters used to image the object) would contain noise and would therefore pose considerable difficulties while restoring the object $f(x,y)$. On the other hand, the use of a PSF computed for the transducer would do away with this issue. The computed PSF can then be further used to study the influence of the various parameters involved in imaging, so that they can be optimized for specific configurations.

This paper is organized as follows: Section II presents the PSF computation in a single medium. It describes how experimental data on a single circular hole as well as on a five-hole cluster in an aluminum calibration block are used to obtain deconvolution-based sizing with the use of a computed PSF. It then details how a calibration curve can be generated for a given transducer which can be used to obtain lateral sizes of unknown objects directly from experimental profiles without the need to deconvolve. Section III presents the computation of the PSF when the transducer is in one medium and the point reflector is in another, with a planar interface separating the two media. It describes how the computed PSF is used with experimental data to deconvolve and determine the lateral sizes of flat-bottom holes (FBHs) in an aluminum calibration block. It also shows that the effective path length concept, used when focused transducers are employed to image subsurface objects, can be applied to evaluate the two-media PSF, thereby simplifying the computation considerably. Section IV presents a discussion on how the PSF and the resulting modulation transfer function (MTF) of planar transducers, spherical focused transducers, and annular transducers can be used to optimize imaging parameters. The paper concludes with a flowchart outlining a procedure for transducer characterization and PSF-based deconvolution. The advantages of having the capability to compute the PSF for any imaging configuration and of the role of the computed PSF in deconvolution-based sizing are highlighted.
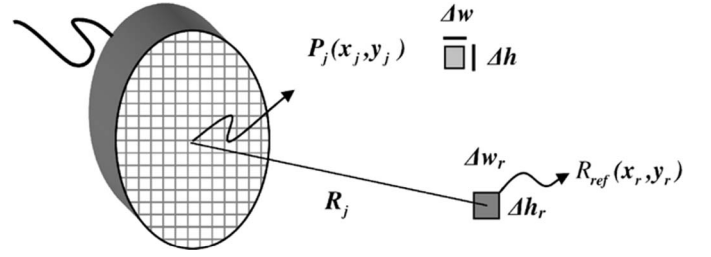

Fig. 1. Schematic of the patch element model (PEM) for transducer field evaluation.

II. CALCULATING THE PULSE-ECHO PSF IN A SINGLE MEDIUM

The PSF can be computed by using a transducer beam model in conjunction with a model that accounts for the back-scattering from a "point" reflector. Several beam models such as the generalized Rayleigh-Sommerfield model [6], the Gaussian beam model [7], [8], and the patch element model (PEM) [9] have been proposed to calculate the incident fields (of transducers) in the frequency domain. Krishnamurthy et al. [10] have used the PEM to determine the transducer field characteristics. The PEM was also used to quantify the FBH response by treating the reflector as made up of patches [10]. The PSF evaluator described below follows a similar approach in that the PEM is used for computing both the transducer fields and the response of a small finite-sized reflector that represents a "point" reflector. The geometry for the model is shown in Fig. 1. The symbols used (other than those already shown in Fig. 1) are a - transducer radius, ω - frequency, λ - wavelength, k - wave number, ΔA - patch area, ρ - density of the medium, c - velocity of sound in the medium, and $i = \sqrt{-1}$.

The transducer is tiled using M patches, a number large enough so that the reflecting point (R_{ref}) lies in the far field of each patch P_j of the transducer (and not necessarily in the far field of the transducer), i.e.,

$$R_j \geq \frac{\Delta w^2}{4\lambda}. \qquad (5)$$

A constant F can be defined so that the above condition can be rewritten to compute the dimension Δw of the patches as

$$\Delta w \leq \sqrt{\frac{4\lambda R_j}{F}}. \qquad (6)$$

F denotes a measure of the distance of the patch P_j to the reflecting point (R_{ref}) relative to the near- to far-field transition distance for the patches. A similar relationship is used to determine the dimension Δh.

The point reflector is modeled as a single patch with dimensions $\Delta w_r \times \Delta h_r$.

The incident pressure field on the reflector patch R_{ref} due to the patch P_j, with the normal component of the particle velocity as v_0, can be computed as

$$P_j^{\text{inc}} = \frac{i\rho c v_0 \Delta A}{\lambda R_j} e^{-ikR_j} D_j, \tag{7}$$

where D_j is the directivity of the patch P_j, given by

$$D_j = \text{sinc}\left(\frac{k(x_j - x_r)\Delta w}{2R_j}\right) \text{sinc}\left(\frac{k(y_j - y_r)\Delta h}{2R_j}\right). \tag{8}$$

For simplicity, the patches have all been chosen to be of the same dimension.

The product of the incident pressure field p_j^{inc} and the directivity function of the reflector patch gives the pressure field received by the patch R_{ref}. The total pressure field at the reflector patch is computed as

$$p_{\text{ref}}^{\text{rec}} = \sum_{j=1}^{M} p_j^{\text{inc}} D_j^r, \tag{9}$$

where D_j^r is the directivity of the reflector patch, given by

$$D_j^r = \text{sinc}\left(\frac{k(x_j - x_r)\Delta w_r}{2R_j}\right) \text{sinc}\left(\frac{k(y_j - y_r)\Delta h_r}{2R_j}\right). \tag{10}$$

The reflector patch is now considered to be a secondary source, and the transducer patches are now thought of as receiver patches. By following the procedure detailed above, the field received by the transducer (p_{rec}) is computed through integration (summation) of the fields received by each transducer patch:

$$p_{\text{rec}}(\omega) = \frac{1}{S} \int_S p_{\text{ref}}^{\text{rec}} A(\omega) \frac{e^{-ikR_j}}{R_j} dS, \tag{11}$$

where $A(\omega)$ is the angle dependent "scattering amplitude" of the reflector represented by

$$A(\omega) = \frac{\Delta w_r \Delta h_r}{\lambda} D_j^r. \tag{12}$$

Once again, the evaluation of the integral is carried out using the patch model.

The term p_{rec}, when evaluated for different relative positions of the transducer and the reflector patch, yields the PSF. For example, the point reflector can be kept fixed on the Z-axis and the transducer moved in the X-Y plane. Then,

$$\text{PSF} = p_{\text{rec}}(x, y). \tag{13}$$

Henceforth, all experimental images referred to shall be understood to have been scanned with a scan step of 0.1 mm in both X and Y directions. This choice will be justified in a later section where scan step considerations are discussed.

A. Imaging with a Planar Transducer

A commercial immersion-type planar transducer, marked 0.375-inch diameter and 5-MHz center frequency,
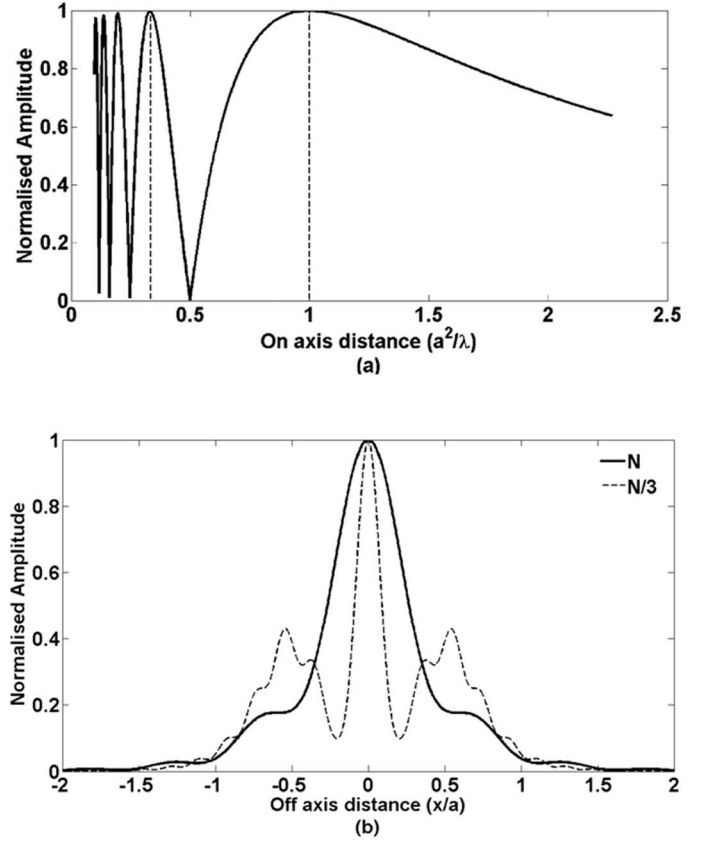

Fig. 2. (a) Computed on-axis response for a circular transducer; (b) comparison of PSFs at N and $N/3$.

was chosen for imaging. Experiments in conjunction with PEM calculation using small reflectors of known size (comparison of pressure profiles along and across the axis of the transducer) led to the determination of the center frequency as 4.9 MHz and the effective diameter as 0.385 inch. The PEM calculations were carried out with the transducer tiled using 3228 square patches with $F = 1300$ for $R = N/3$, where $N = a^2/\lambda$ is the near- to far-field transition distance for the transducer. Such a value of F ensured that the reflector patch was in the far field of each transducer patch.

Consider a point reflector and a transducer placed such that the reflector lies fixed at some point along the axis of the transducer. Henceforth, we shall refer to the "on-axis" response of the reflector as the pressure field measured when the transducer is translated along its axis. Similarly, by "off-axis" response, we refer to the pressure field measured by translating the transducer perpendicular to its axis.

The normalized on-axis response of a point reflector for a planar transducer computed using PEM is shown in Fig. 2(a). Since the on-axis distance has been scaled by the transition distance N, the curve shown is independent of the choice of a and λ. The two imaging distances of interest for the planar transducer are the transition distance N and the near field distance $N/3$. The PSFs at these two distances are shown in Fig. 2(b). Despite the high sidelobe levels, imaging at $N/3$ is of interest because of the narrower

beam width compared to the beam width at N. Imaging at distances closer than $N/3$ is not considered because of the lack of a distinct main beam at such close distances.

Remark: The off-axis response at the same characteristic distance of transducers, when scaled by the respective transducer radii, becomes independent of the choice of the transducer parameters, i.e.,

$$\text{PSF}\left(\frac{x}{a_1}, \frac{y}{a_1}, z = q \cdot N_1\right)_{\text{Transducer 1}}$$
$$= \text{PSF}\left(\frac{x}{a_2}, \frac{y}{a_2}, z = q \cdot N_2\right)_{\text{Transducer 2}}. \quad (14)$$

Hence, the PSFs shown in Fig. 2(b) are universal and indicate that $N/3$ is always a better imaging distance than N for planar transducers.

B. Restoring Images in a Single Medium

The 2-D Wiener deconvolution procedure in MATLAB (The MathWorks, Inc., Natick, MA) was used to restore images as

$$F(u,v) = \frac{G(u,v) \times \overline{H}(u,v)}{K + |H(u,v)|^2}, \quad (15)$$

where $\overline{H}(u,v)$ is the complex conjugate of $H(u,v)$, and K, usually a fraction of $|H(u,v)^2|$, is introduced to prevent spurious enhancement caused by zeroes of $|H(u,v)^2|$.

1. Imaging at Distance N: Fig. 3(a) and (b) show the experimental and restored images of a 1.5-mm-diameter hole in an Al 7075-T6 calibration block. The experimental image shows the dimension of the hole to be much larger than the actual size due to the blurring effect of the PSF. Diametrical profiles of the experimental and restored images are shown in Fig. 4(a) and (b). Similarly, Fig. 5(a) and (b) show the experimental and restored images of a section of the calibration block having five 1.5-mm-diameter holes arranged along a 10° incline. The spacing between consecutive holes is 4 mm, 4 mm, 2.5 mm, and 2.5 mm. The closest separation between two points that need to be resolved is hence 1 mm. It can be seen from Fig. 5(a) that the closer holes are nearly indistinguishable. Fig. 6(a) and (b) show the profiles across the holes from the experimental and restored images. The restored profile does show five holes, though not well resolved.

2. Imaging at Distance $N/3$: The single hole and the five-hole cluster imaged at N were also imaged at $N/3$. Fig. 7(a) and (b) shows the experimental and restored images of the single hole imaged at $N/3$. The high sidelobe level in the PSF manifests as a ring-like structure in the experimental image. The diametrical profiles for the two images are shown in Fig. 8(a) and (b), respectively. The dimension of the single hole is reproduced almost exactly. The experimental and restored images of the five-hole cluster are shown in Fig. 9(a) and (b). The profile
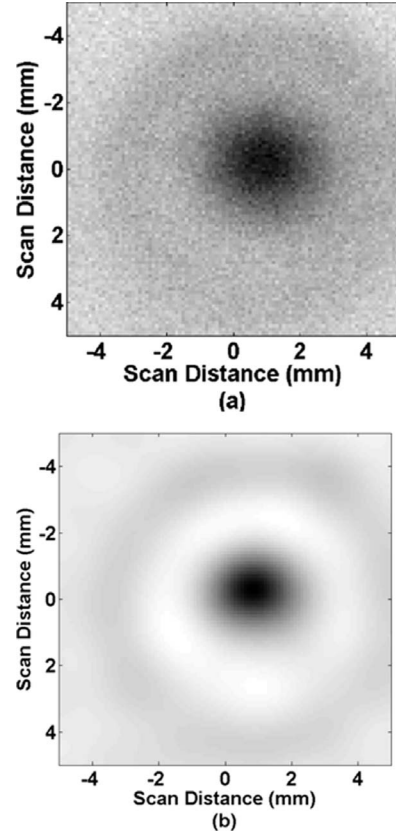

Fig. 3. (a) Experimental image of a 1.5-mm-diameter hole in an Al calibration block using a 0.375-inch, 5-MHz transducer at N; (b) image restored using the computed PSF.

across the holes is shown in Fig. 10(a) and (b). From the profile, the spacing between consecutive holes was found to be 4 mm, 4.3 mm, 2.3 mm, and 2.4 mm, which compare well with the actual values. Three hundred iterations of the Lucy-Richardson deconvolution algorithm in MATLAB were found to resolve the five-hole cluster and size the holes with good accuracy.

C. Calibration Curve for Circular Reflectors

Recall the remark made in Section II-A that (at a given characteristic on-axis distance) the PSF beam width scales as the transducer radius a. Hence, C-scans can be used directly to get the size of flaws if they are of the order of a. However, this would not be the case for smaller flaws, where the modifying influence of the PSF is much greater, causing the experiment to only give an apparent size. We demonstrate below that we can make use of this difference in the influence of the PSF to calculate the actual sizes of small flaws. We use the 0.375-inch circular transducer to image circular reflectors in water with the imaging distance as N. For this purpose, the PSF for the transducer is computed at distance N and convolved with circular reflectors having diameters ranging from one-tenth to 2 times the transducer diameter to calculate the profile of the reflectors that we would get from an experiment. From these profiles, we observed that the true sizes of reflectors larger than the transducer were indicated at 6.85 dB. This infor-
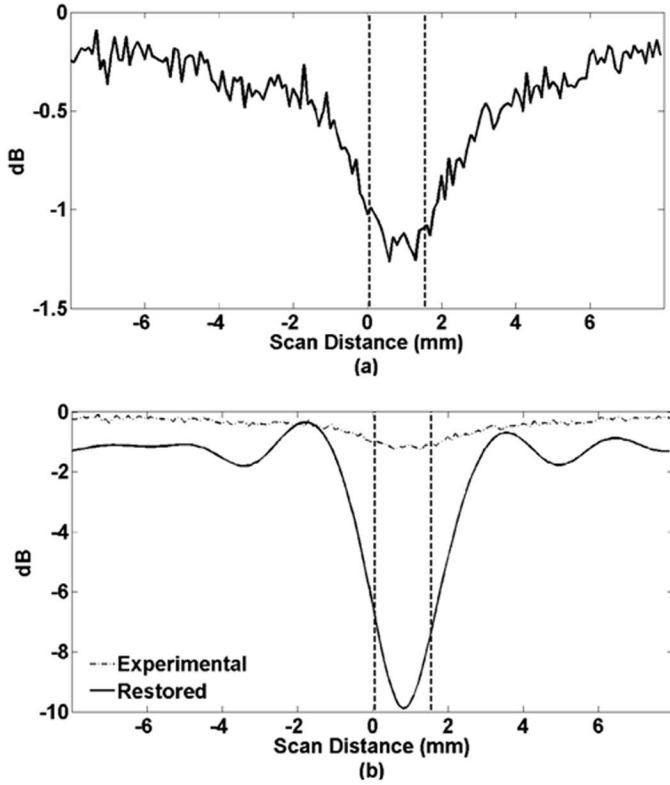
Fig. 4. (a) Diametrical profile across experimental image and (b) across the restored image for the single-hole case. The profile after restoration provides a much better measure of the size of the hole (marked by vertical lines) compared to the profile from the experiment.
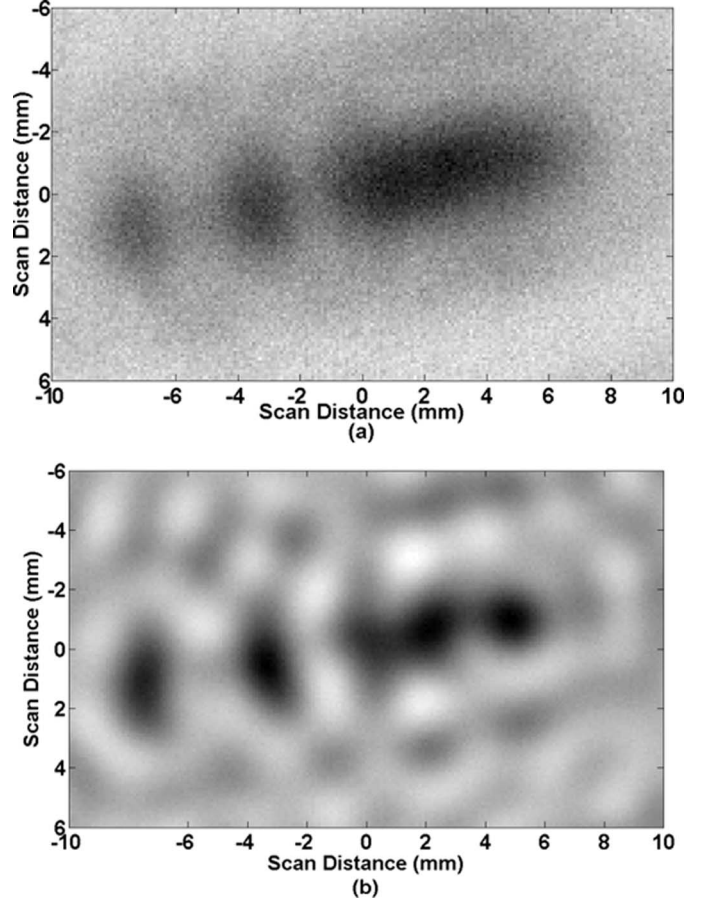

Fig. 5. (a) Experimental image of Al block having 5 holes; (b) restored image. Notice the poor resolution of the holes with close spacing. This occurs due to the high beam width at N.

mation is used to draw a calibration curve which maps the apparent width of the reflectors at 6.85 dB (measured from an experiment) to the actual diameters of the reflectors. To keep the curve *universal* (i.e., imaging at N using any planar transducer), the apparent and actual widths are scaled by the transducer diameter. Fig. 11 shows a plot of the scaled apparent sizes of reflectors at 6.85 dB versus their corresponding scaled actual sizes. To demonstrate the use of this curve, the 6.85 dB width of the experimental profile of an $8/64$-inch FBH in the calibration block was measured to be 0.172 inch. Using the calibration curve, the size was read as 0.128 inch, which compares very well with the actual size. We suggest that the effective diameter (as opposed to the marked diameter) of the transducer found after calibration be used to draw this curve. The physical (/marked) diameter does provide a reasonable approximation for reflector sizing.

III. PSF CALCULATIONS IN THE PRESENCE OF A PLANAR INTERFACE

Restoration of subsurface images necessitates the calculation of PSFs in the presence of an interface. Fig. 12 shows the relevant schematic for this calculation. The procedure to compute the PSF is outlined here.

The transducer is tiled with a number of patches following the criterion described in Section II. The distance to be used to decide M should now be the depth of the interface instead of the distance to the reflector patch.

Each patch is treated as an effective point source and the high frequency approach employing a ray picture is utilized for determining the field across the planar interface [11].

A ray is traced from the transducer patch P_j to the reflector patch R_{ref} using Snell's law.

Defining $n = c_1/c_{p2}$, D_j as the directivity of the transmitting patch, $T_{12}(\theta)$ as the transmission coefficient from medium 1 to medium 2, $s_{1,j}$ as the length of the ray from the patch P_j to the interface, and $s_{2,r}$ as the length of the ray from the interface to the patch R_{ref}, the component of the incident displacement field on R_{ref} due to patch P_j is computed as

$$u_j^{\mathrm{inc}}(R_r) = \frac{-i\rho_1 v_0}{\rho_2 c_{p2}}$$
$$\cdot \frac{T_{12}(\theta_{\mathrm{inc}}) \exp(ik_1 s_{1,j} + ik_2 s_{2,r}) \cdot D_j}{\sqrt{s_{1,j} + \dfrac{s_{2,r}}{n}} \cdot \sqrt{s_{1,j} + \dfrac{\cos^2(\theta_{\mathrm{inc}})}{n\cos^2(\theta_{\mathrm{refr}})} s_{2,r}}}. \quad (16)$$

Analogous to the computation in a single medium, the incident displacement field at the patch R_{ref} is then computed as
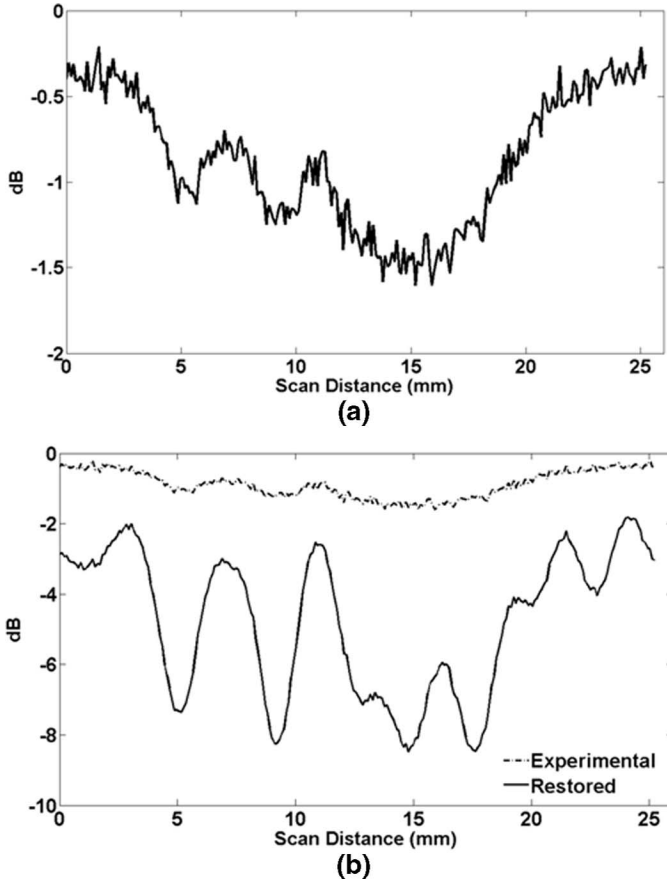
Fig. 6. (a) Profile (along the line passing through the center of the holes) across the holes in the experimental image and (b) across the restored image of the five-hole section.
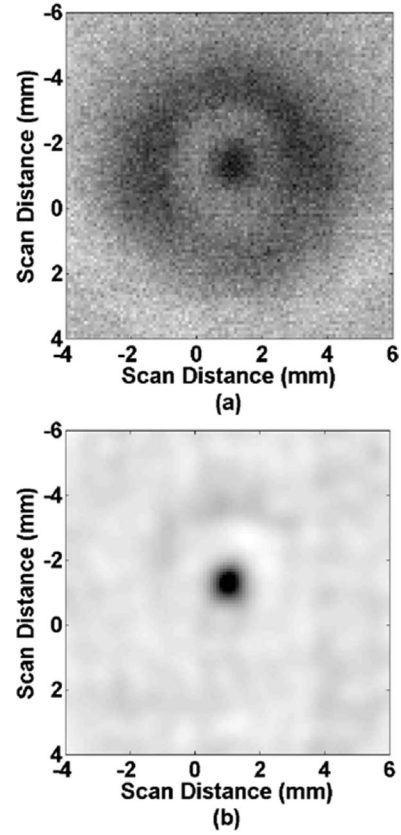

Fig. 7. (a) Experimental image and (b) restored image of the single hole when the imaging takes place at a near-field distance $N/3$. The ring-like structure in the experimental image occurs due to the high sidelobe level at this imaging distance.

$$u_{\text{ref}}^{\text{rec}} = \sum_{j=1}^{M} u_j^{\text{inc}} D_j^r, \tag{17}$$

with D_j^r defining the directivity of the reflector located in the second medium.

Once again, R_{ref} is considered to be a secondary source. Rays are traced from the second medium back into the first, received by each patch of the transducer, and integrated (summed) over the transducer area to obtain the received field:

$$p_{\text{rec}}(\omega) = \frac{i\omega\rho_2 c_{p2}}{S}$$
$$\cdot \int_S \frac{u_{\text{rec}}^{\text{ref}} A(\omega) T_{21}(\theta_{\text{inc}}) \exp(ik_1 s_{1,j} + ik_2 s_{2,r})}{\sqrt{s_{2,r} + n s_{1,j}} \cdot \sqrt{s_{2,r} + \dfrac{n\cos^2(\theta_{\text{refr}})}{\cos^2(\theta_{\text{inc}})} s_{1,j}}} dS, \tag{18}$$

where $A(\omega)$ is, as before, the "scattering amplitude" of the reflector located in the second medium and is represented by the "$\sin c$" functions. The evaluation of (17) is carried out using the patch model.

A. Experimental Verification of PSF Calculations for a Water-Aluminum Interface

Time-gated flaw signals from experiments using an Al 7075-T6 calibration block having $3/64$-inch-diameter FBHs

at different depths were used to verify the PSF calculations in the presence of an interface. Fig. 13(a) shows the experimental and computed on-axis response from the FBH at a depth of 0.3 inch from the interface and a varying water path. From the experiments and the PEM calculations, the center frequency of the transducer was found as 4.9 MHz and the effective diameter as 0.385 inch. Fig. 13(b) and (c) show the experimental and computed diametrical profiles of the FBH for two different water patches corresponding to a near-field distance and the transition distance (the last on-axis maxima in the pressure field). Since the $3/64$-inch FBH could not be considered as a single patch, it was modeled as a circular reflector discretized into Q patches, $R_{\text{ref},q}$. Alternatively, the computed profile could also have been calculated by convolving the PSF with a function representing the FBH.

B. Restoring Subsurface Images

With the PSF calculation verified (by good agreement) with experiments and the effective diameter of the transducer found as 0.385 inch, the computed PSF was used to restore images of $5/64$-inch- and $8/64$-inch-diameter FBHs at a depth of 0.4 inch in the Al calibration block. The water path was 33.7 mm so as to have the FBH at the location of the last on-axis maximum in the pressure response. The
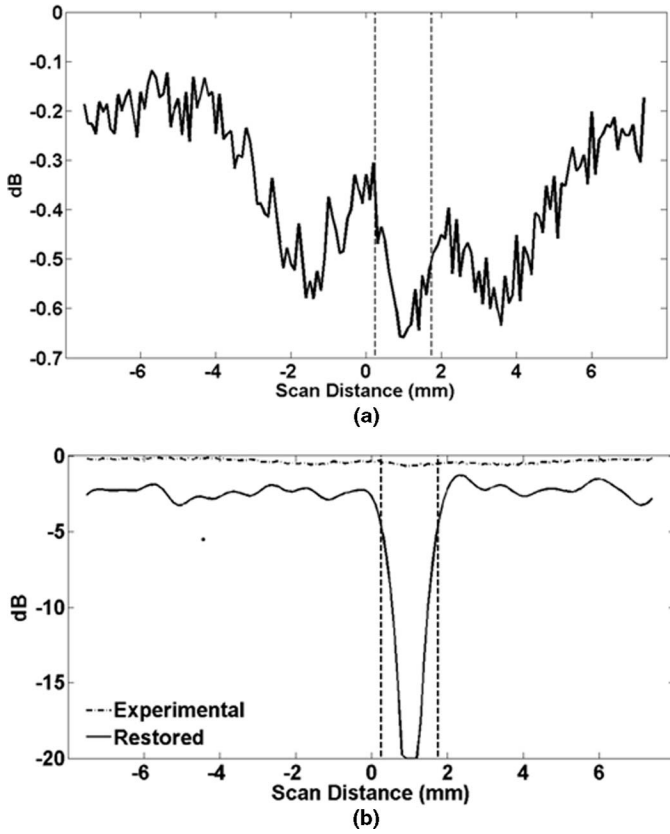
Fig. 8. (a) Diametrical profile across the experimental image and (b) profile across the restored image for the single hole. The dotted line indicates the actual size of the hole. The restored image gives the nearly exact size of the hole.

Fig. 9. (a) Experimental image of the five-hole section and (b) the restored image. Hole sizing should be done using the diametrical profiles.

experimental and restored images (using the Wiener deconvolution) of the $5/64$-inch FBH are shown in Fig. 14(a) and (b). Their respective diametrical profiles are shown in Fig. 14(c). The exercise was repeated for the $8/64$-inch FBH. The corresponding images and profiles are given in Fig. 15(a)–(c). The restoration is seen to be good for both cases.

C. Replacing Aluminum with an Effective Water Path

It is a common practice to find the focusing depth of spherical focus transducers in the presence of a second medium (say, Al) using an effective path length concept [5] as

Depth of focal point in Al =

$$\text{(focal length} - \text{water path)} \cdot \frac{c_{\text{water}}}{c_{p,\text{Al}}}. \quad (19)$$

The PSF calculator was used to evaluate such a rule of thumb in the context of imaging. The locations of the maxima at N and at $N/3$ (analogous to the focal length for a spherical focus transducer) in water alone and in the presence of an Al interface for a 0.375-inch-diameter, 10-MHz planar transducer are compared in Table I. Fig. 16(a) and (b) compare the PSFs using single-medium (with effective path length) and two-medium calculations for distances
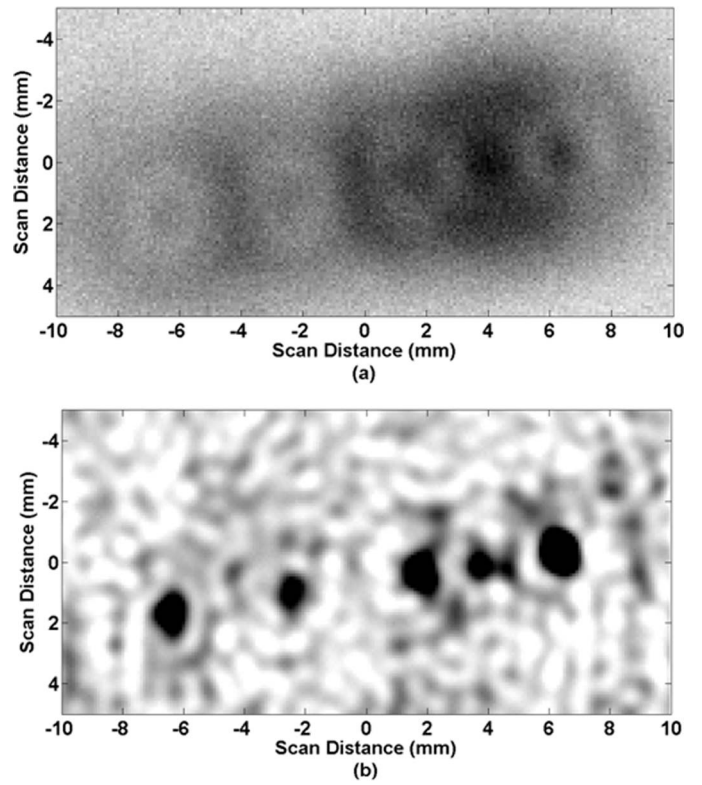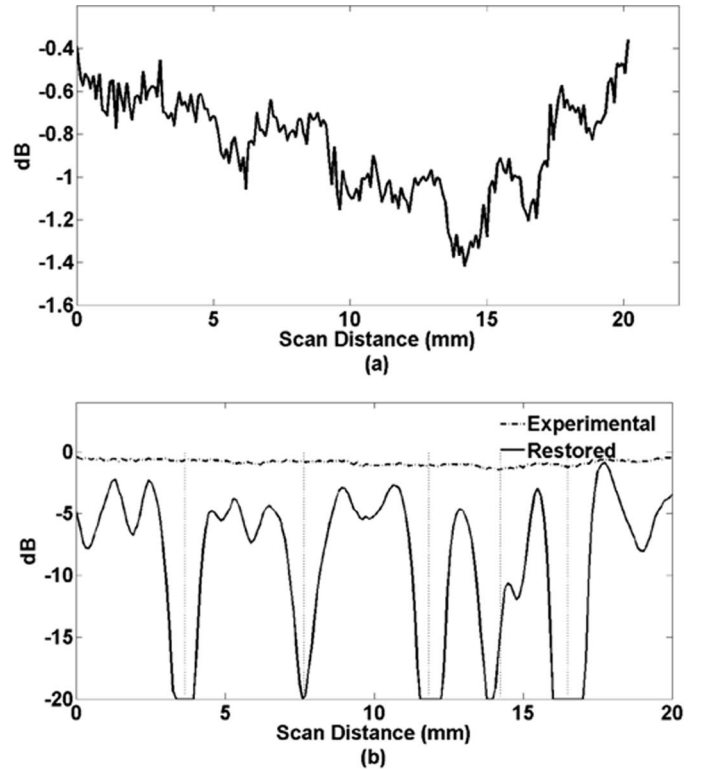

Fig. 10. (a) Profile across the experimental image and (b) across the restored image. The locations of the holes are indicated using dotted lines. Notice that all the holes are well resolved and that the holes farther apart are better resolved than others.

TABLE I
Comparison Between 2-Medium and Effective Path Length Calculations.

Symbol	Water (single medium)	15-mm water path + Al interface
Depth of maximum at $N/3$	51.47 mm	23.15 mm
Depth of maximum at $N/3$ (Thumb rule)	N.A.	$15 + (51.47 - 15) \times \left(\dfrac{1.47}{6.32}\right) = 23.48$ mm
Depth of maximum at N (PEM model)	154.40 mm	47.30 mm
Depth of maximum at N (Thumb rule)	N.A.	$15 + (154.4 - 15) \times \left(\dfrac{1.47}{6.32}\right) = 47.43$ mm
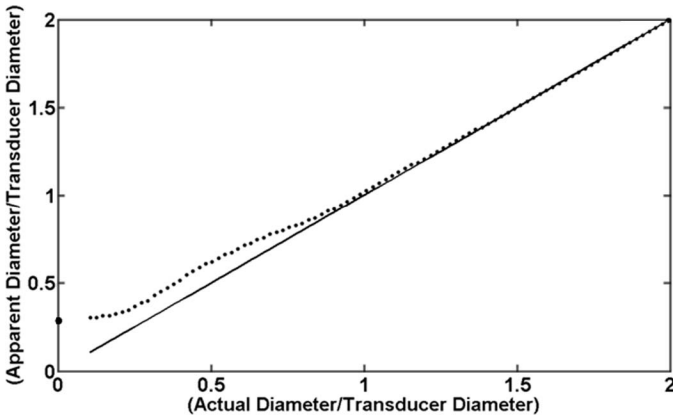
Fig. 11. Calibration curve for imaging with planar transducers at N. The curve gives the actual sizes of circular reflectors from their apparent sizes indicated by the 6.85 dB level. The apparent width of a point reflector (6.85 dB width of the PSF) is also marked on the ordinate axis.
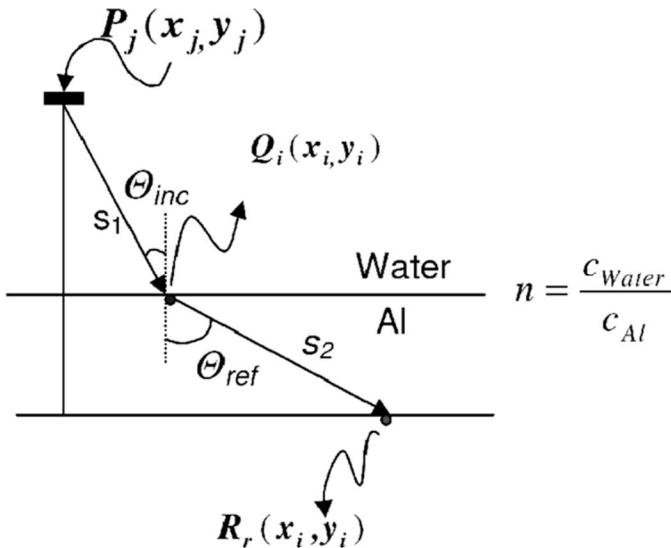

Fig. 12. Schematic for field evaluation across a planar interface for an elemental patch of the transducer.

N and $N/3$, respectively. The close correspondence even in the far sidelobe regions indicates that the thumb rule is indeed a good approximation for imaging and sizing in both the near and the far field.

IV. Influence of Imaging Parameters

The transducer shape and diameter, the imaging distance, and the scan step are the imaging parameters considered for discussion. We have demonstrated that $N/3$ was a superior imaging distance for the planar transducer compared to N. We proceed to study the PSF characteristics of the spherical focus and annular transducers, widely used for imaging, to find favorable imaging distances.

A. Spherical Focus Transducers

It is well known that spherical focus transducers focus ahead of their geometric focus [8]. This can be seen in Fig. 17(a), where the true focus (henceforth referred to as TF) of a 0.375-inch-diameter, 5-MHz center frequency spherical focus transducer was found to be 0.6 R_0, significantly ahead of the geometric focus (GF) $R_0 = 77.2$ mm.

Remark: With a fixed geometric focal length R_0, the family of spherical focus transducers with the same value of $N = a^2/\lambda$ would have the same true focal length.

Fig. 17(b) compares the PSF at the TF and the GF. The PSF at the TF is seen to be narrower than at the GF, and this was found (and can be shown) to happen for any spherical focus transducer. This clearly suggests that the TF is always a better imaging distance than the GF. We observed that for a fixed focal length, a larger aperture and/or a smaller wavelength not only shifted closer to the GF, it also improved the PSF (by narrowing the beam width) at the corresponding locations of the TF. A similar shift can be achieved, instead, by reducing the focal length for fixed a and λ.

B. Annular Transducers

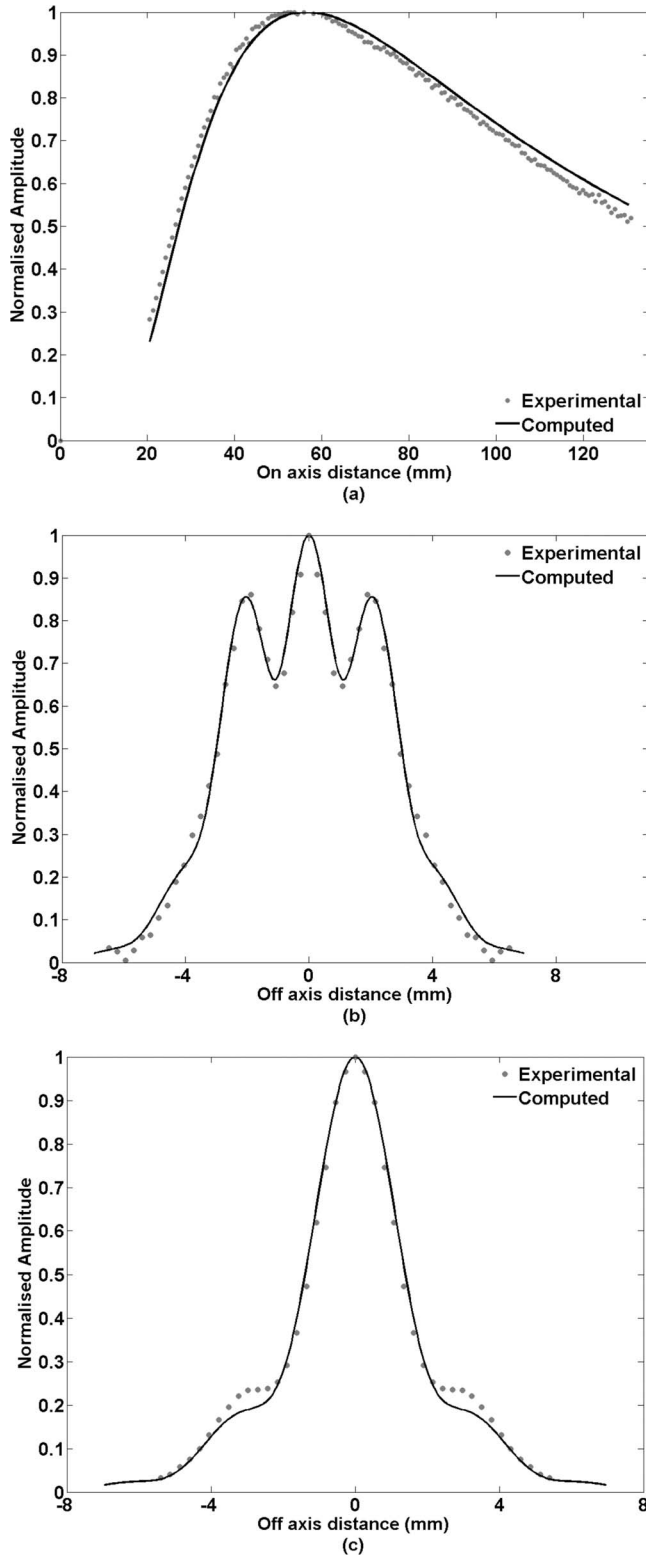Annular transducers are considered attractive for imaging purposes due to the non-diffracting beams that they

Fig. 13. (a) On-axis response from a $3/64$-inch FBH at 0.3-inch depth in Al and a variable water path. The computed profile used an effective diameter of 0.385 inch, different from the 0.375 inch marked on the transducer. Experimental and computed diametrical profiles of the FBH at (b) a near-field distance (20.3-mm water path and 0.3-inch Al path), and (c) the transition distance from near to far field (46-mm water path and 0.3-inch Al path). The computations agree well with the experiment in all three cases.
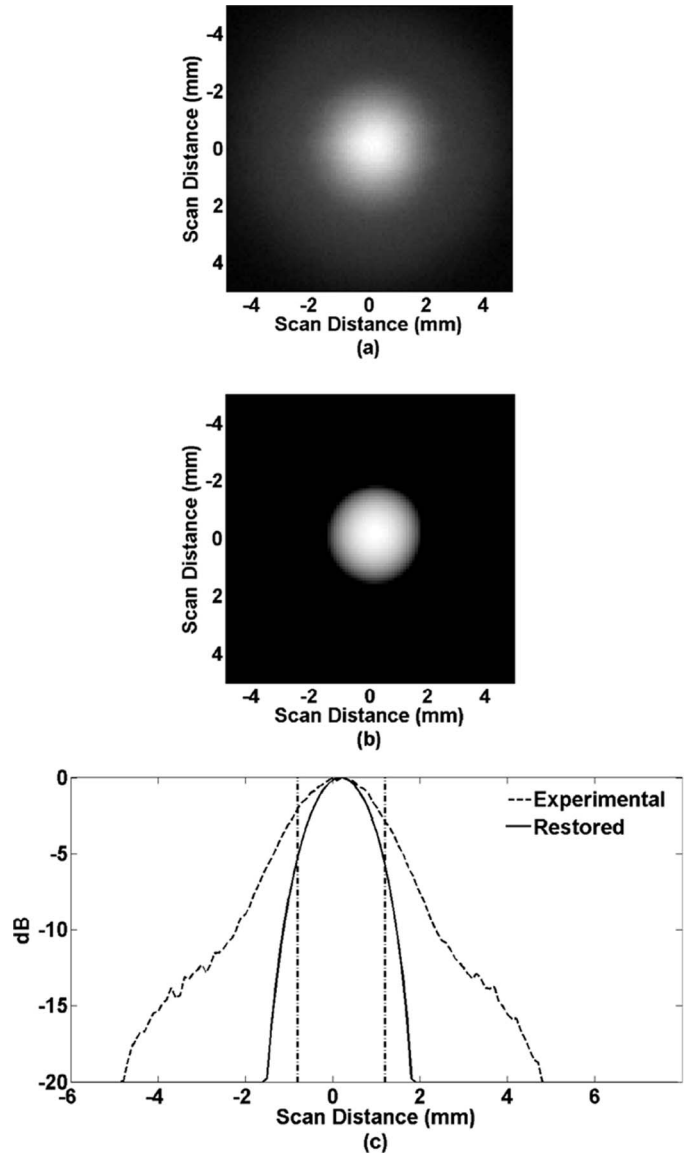
Fig. 14. (a) Experimental image, (b) restored image, and (c) diametrical profile of a $5/64$-inch FBH at a 0.4-inch depth in Al. The water path was 33.7 mm, corresponding to the transduction distance for the transducer. The exact size of the FBH is shown in dotted lines.

can generate [12], [13]. They are specified by their inner and outer diameters and the center frequency. We exploit the fact that if the radii for the annulus are chosen using the idea of Fresnel zones [14], these transducers can "focus" the energy at a desired point along the axis. Thus, for a fixed inner radius a_{in}, the outer radius a_{out} is chosen so that the difference in path length from these two radii to the focal point at F_0 is $\lambda/2$, i.e.,

$$\sqrt{a_{\text{out}}^2 - R_0^2} - \sqrt{a_{\text{in}}^2 - R_0^2} = \lambda/2. \qquad (20)$$

Such a choice ensures that all waves emanating from the annulus interfere constructively (though not completely constructive, as in the case of the spherical focus transducer).
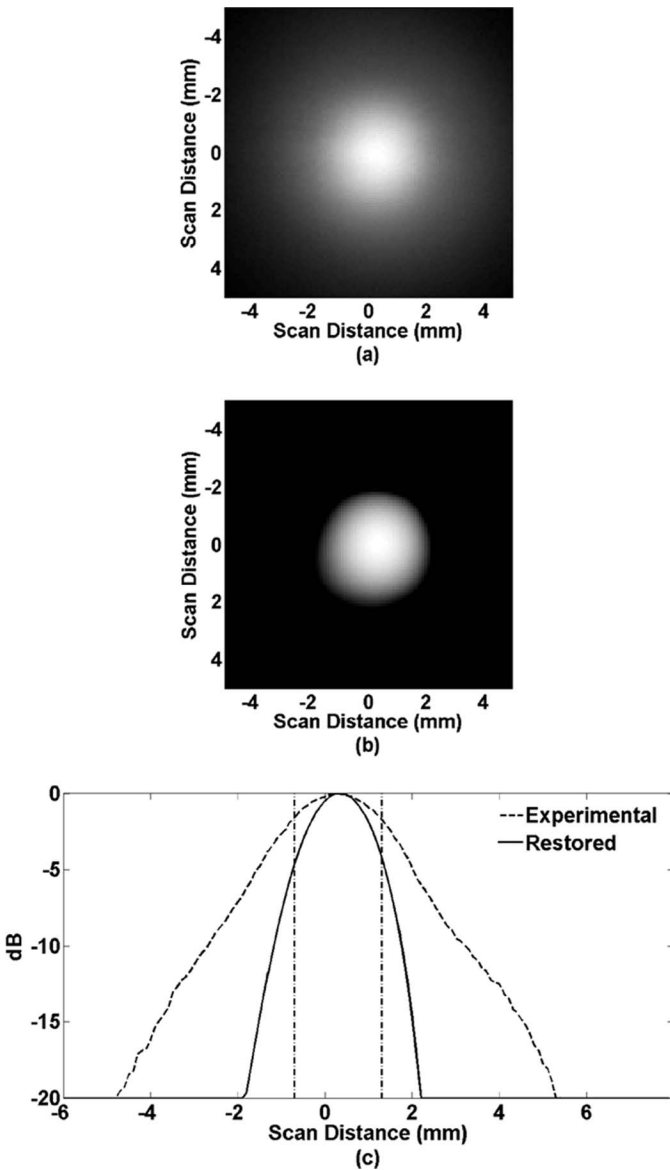
Fig. 15. (a) Experimental image, (b) restored image, and (c) diametrical profile of an $^8/_{64}$-inch FBH. The depth in Al and water path is the same as the $^5/_{64}$-inch FBH case. The exact size of the FBH is indicated by dashed vertical lines.
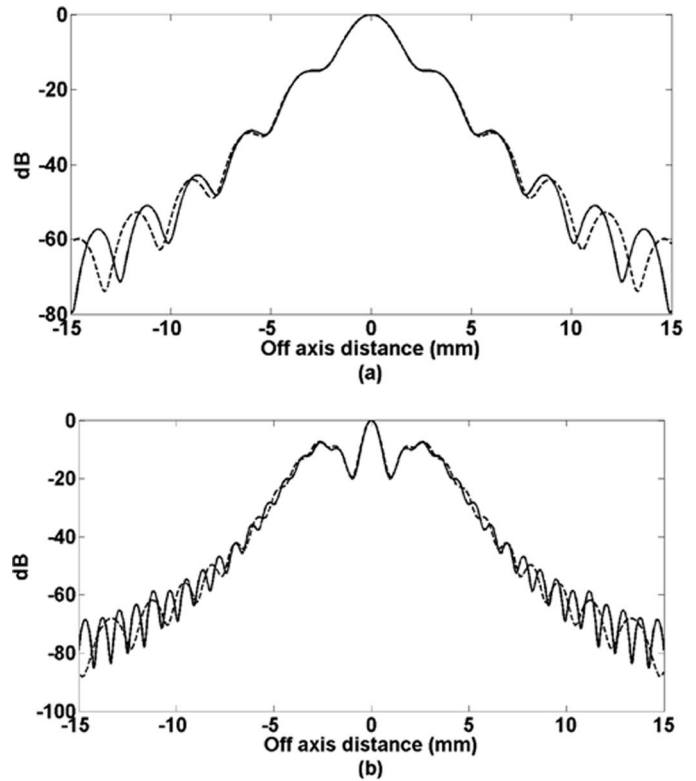

Fig. 16. Comparison between the exact two-medium PSF calculation (solid line) and the effective single-medium PSF calculation (dashed line). (a) PSFs at $N/3$, and (b) PSFs at N. The dB scale was adopted to enable comparison of the sidelobes far from the axis of the transducer.

is narrower than the PSF at N for the planar transducer. The same is the case at $R_0/3$ and $N/3$, respectively, but the sidelobe level for the annular transducer is much less than for the planar transducer at their respective imaging distances. Hence, the annular transducer would be better suited for imaging than the planar transducer.

Remark: For a particular choice of the focal length as $a_{in}^2/\lambda(= N_{in})$, the PSF (at any characteristic distance) scaled by a_{in} was a profile independent of a_{in} and λ.

For a fixed focal length, the PSF at the focal length can be improved by increasing the inner diameter (and calculating the appropriate outer diameter) and/or by increasing the frequency. *Interestingly*, we found that for the annular transducer, the penultimate maximum in the on-axis response occurs very close to $R_0/3$, and the PSF at this distance had a significantly narrower beam width than at R_0, which bears a striking similarity to the results for the planar transducer. The decrease in beam width is accompanied by an increase in the sidelobe. Fig. 18(a) and (b) compares the PSFs for the planar and annular transducers. Clearly, the PSF at R for the annular transducer

C. Image Resolution Capabilities

The resolution that a transducer achieves can be deduced by evaluating its MTF. The MTF gives the relative amplitude of the different *spatial frequency* components of the PSF and can hence be directly associated with resolving capability [4] of the system. For a spatial frequency approaching 0 (two points separated by very large distances), all imaging configurations provide a relative contrast of ~1 (100%) since the two objects would be completely resolved. As the spatial frequency increases, i.e., as objects get closer to each other, the resolving capability of the system decreases. Fig. 19 shows a comparison of MTF curves for the planar transducers (parameters: a and λ) and annular transducers (parameters a, λ, and $R_0 = a^2/\lambda$) at N. The resolving capability of a transducer can be nominally taken to be the spatial frequency for which the MTF indicates 50% contrast. In Fig. 6(a), the 4-mm-spaced holes (2 holes separated by a 2.5-mm gap) are well resolved while the 2.5-mm-spaced holes (three holes separated by 1-mm gaps)
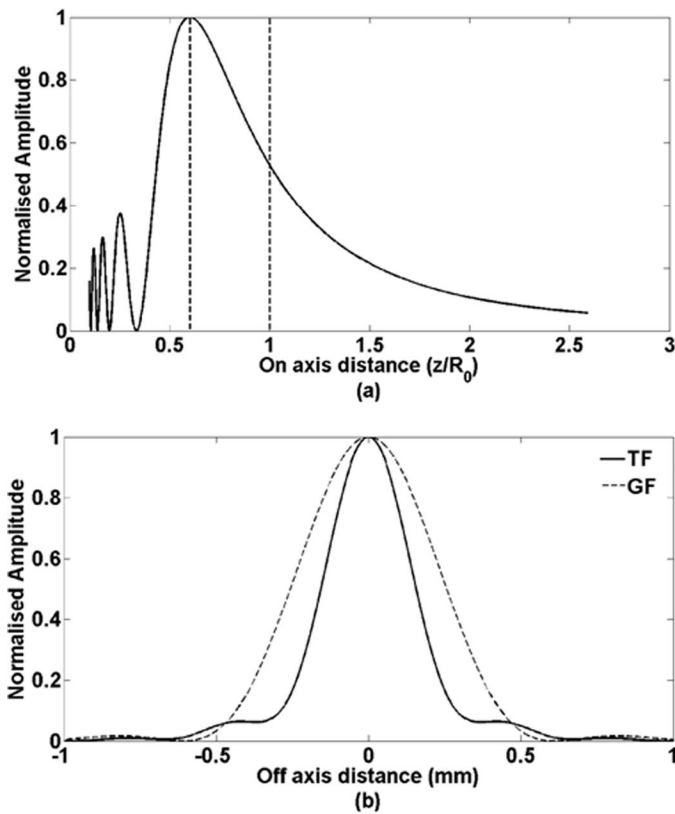
Fig. 17. Characteristics of a spherical focus transducer. (a) On-axis response of a point reflector showing the true and geometric focal lengths; (b) PSFs at these two distances.
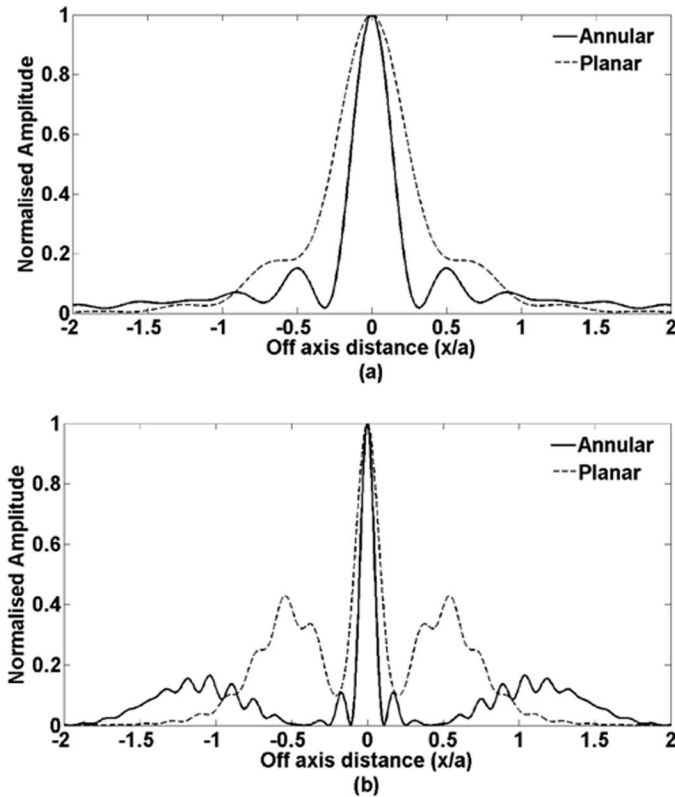

Fig. 18. Comparison of the PSFs of annular and planar transducers at (a) N and at (b) $N/3$.
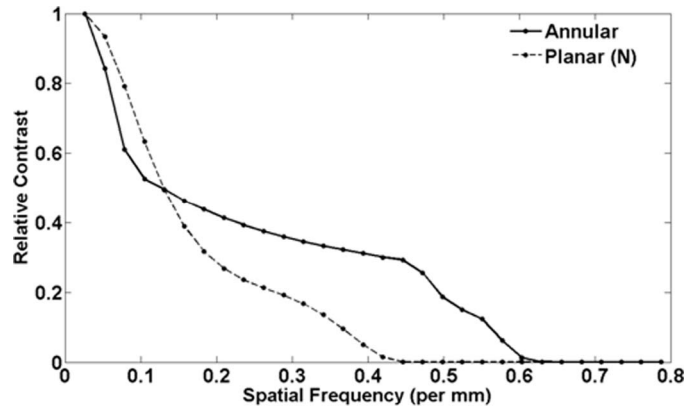

Fig. 19. Comparison of MTF curves for the planar and annular transducers at N. The inner radius of the planar transducer is equal to the radius of the planar transducer.
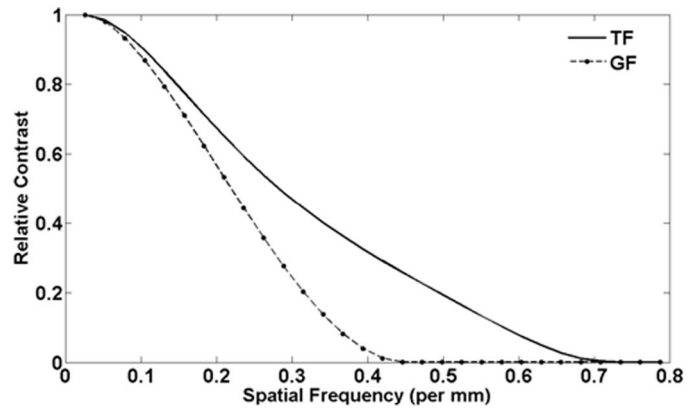

Fig. 20. Comparison of MTF curves at the geometric and true focal distances of a spherical focus transducer of radius 0.375 inch, center frequency 5 MHz, and focal length 77 mm.

are unresolved. This can be understood from the MTF response for the planar transducer. The 4-mm-spaced holes can be thought of as corresponding to approximately 0.3 lines/mm, leading to a 20% contrast. The 2.5-mm-spaced holes can be thought of as corresponding to approximately 0.5 lines/mm, leading to vanishing contrast.

It can be seen how the annular transducer provides a much higher contrast for closely spaced objects. Fig. 20 compares the MTF curves at the TF and the GF of the spherical focus transducer used in Section VIII-A, quantitatively proving that the TF is a better imaging distance. The MTF for the planar and annular transducers at $N/3$ are not shown since the spatial frequency components of the sidelobes interfere with those of the main lobe (the portion of the beam which is of interest for imaging). However, in practice, the advantages of the planar and annular transducers at $N/3$ should be exploited.

Although the contrast decreases at higher spatial frequencies, systems based on 12-bit or 14-bit data acquisition (DAQ) cards can discriminate lower contrast and provide higher resolutions.

D. Scan Step Considerations

The PSF and the corresponding MTF would represent the transducer characteristics when evaluated with a sufficiently small scan step, say, δ_0. This scan step is arrived at by ensuring that no further detail is revealed in the PSF/MTF by decreasing the scan step further than δ_0. A value of 0.1 mm was found to be reasonable to generate the PSFs for the systems chosen in the present work. From the MTF, it is possible to deduce the scan step required to generate C-scans as follows: Let n be the number of units resolved in an interval of 10 mm at a specified contrast in the MTF. According to the sampling theorem, a minimum of 2 points would be required to sample a unit. Combining these two features, the upper bound on the scan step δ would be given by

$$\delta = \frac{10}{(2 \times n)} \text{ mm.} \tag{21}$$

Since it is known that the number of points m necessary to sample a unit would have to be larger than 2, a finer scan step would result in practice. In general, then, the scan step would be given by

$$\delta = \frac{10}{(m \times n)} \text{ mm.} \tag{22}$$

However, the finest scan step cannot be lower than δ_0, for the transducer characteristics limits the resolving capabilities fundamentally. In other words, given n, increasing m indefinitely does not help resolve the object.

In principle, restoration through deconvolution helps resolve the object even though the object is poorly resolved in the raw image. For instance, in the profile of the raw image shown in Fig. 6(a), the three closely spaced holes appear unresolved. In the profile of the restored image shown in Fig. 6(b), the three holes appear resolved. A fine enough scan step and sufficient contrast in the restored image enabled the three holes to be resolved. The contrast achievable during the restoration process is governed by the noise in the raw image and also the numerical noise introduced by the deconvolution procedure, even if it is assumed that the computed PSF contributes negligible numerical noise.

However, it is important to bear in mind that deconvolution does not automatically ensure that all features in the raw image would be resolved. Suppose the PSF is available at a very fine scan step and the raw image is at a coarse scan step (often due to time and scanner limitations). Because restoration through deconvolution requires the raw image grid and the PSF grid be identical, either that raw image has to be interpolated to match the PSF grid or the PSF grid has to be coarsened to match the raw image grid. Interpolating the raw image can lead to artifacts. Different interpolation schemes may result in producing different nonexisting features in the restored image. Coarsening the PSF grid restricts the resolving capabilities otherwise inherent in the transducer characteristics. Fig. 21 shows the effect of restoring the coarsened raw
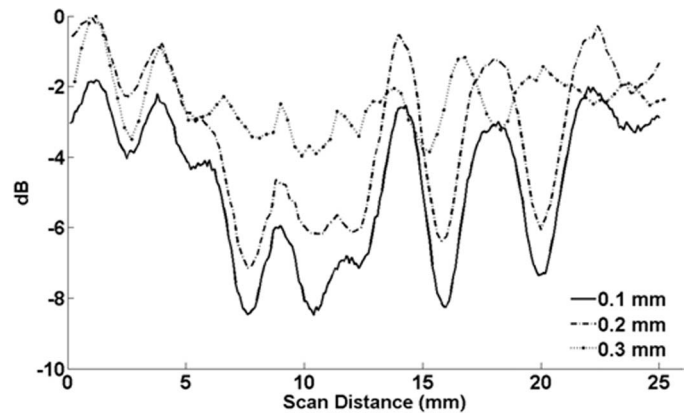

Fig. 21. Reduction in contrast of restored image with coarsening of scan step. The raw image in Fig. 5(a) was coarsened to 0.2 mm and 0.3 mm. The deconvolution was performed using PSFs coarsened to match the corresponding image grid.

image of the five-hole object with appropriately coarsened PSF. It can be seen that the contrast in the images reduces rapidly with increase in scan step.

V. Conclusions

The PSF computation, like transducer characterization, is a one-time procedure to ascertain the resolving capabilities of a transducer. Calculation of the PSF requires characterizing the transducer. Fig. 22 depicts a flowchart indicating a procedure that can be followed (and the one used in this paper) for characterization of planar transducers. Given the transducer parameters, the PSF is evaluated for any specific imaging configuration. Fig. 23 shows a flow chart indicating a procedure that can be used for deconvolution-based sizing, using the PSF for the chosen imaging configuration. It may be noted from Fig. 23 that image restoration is done with time-gated signals and does not require *a priori* knowledge of the flaw depth. Examples of how ultrasound images can be restored and how defects can be sized through deconvolution using the computed PSF with minimal noise have been discussed. We also note that the capability of evaluating the PSF helps imaging parameters such as imaging distance, scan step, and frequency to be optimized for a variety of apertures and apodizations. The medium in which the beam is launched and collected is found to determine the PSF even in cases where the flaws need to be imaged across planar interfaces separating two media. In addition to the commonly encountered immersion-based imaging, contact mode imaging with wedge- or roller-based transducers would also benefit from this feature as it simplifies the PSF computation. The PSF evaluator in this paper is general, capable of handling array configurations and/or newer imaging configurations that may lead to possibly higher lateral resolutions in the near field as well as in the far field. Experiments using other transducer configurations such as the phased array and the focused transducer are underway.
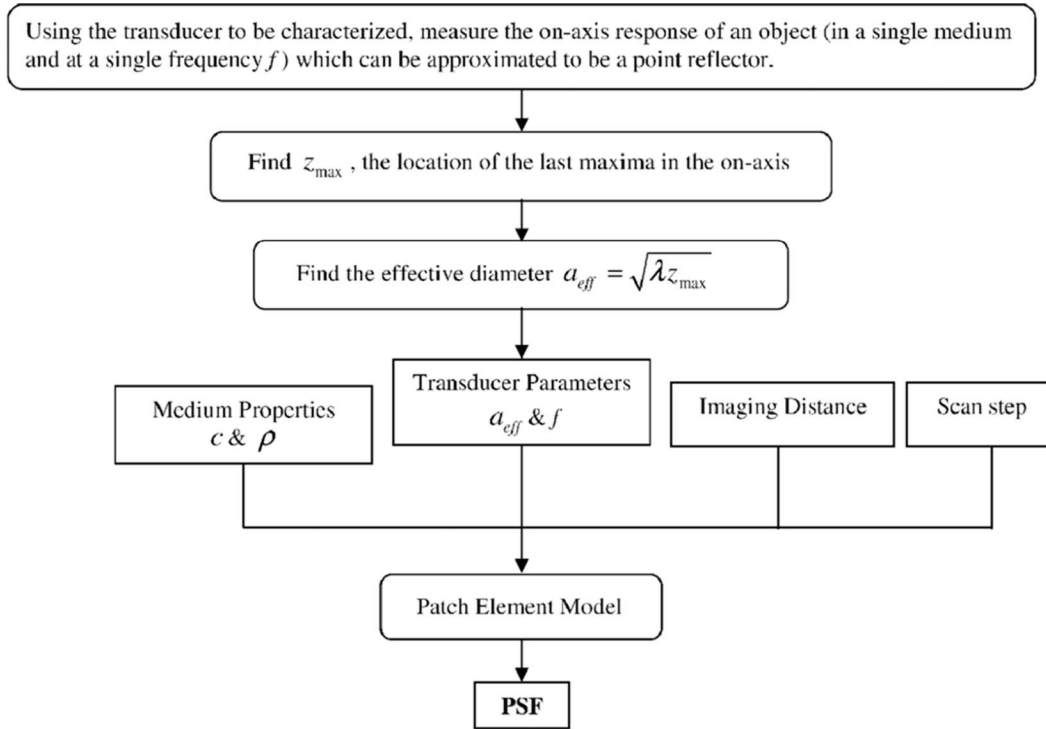
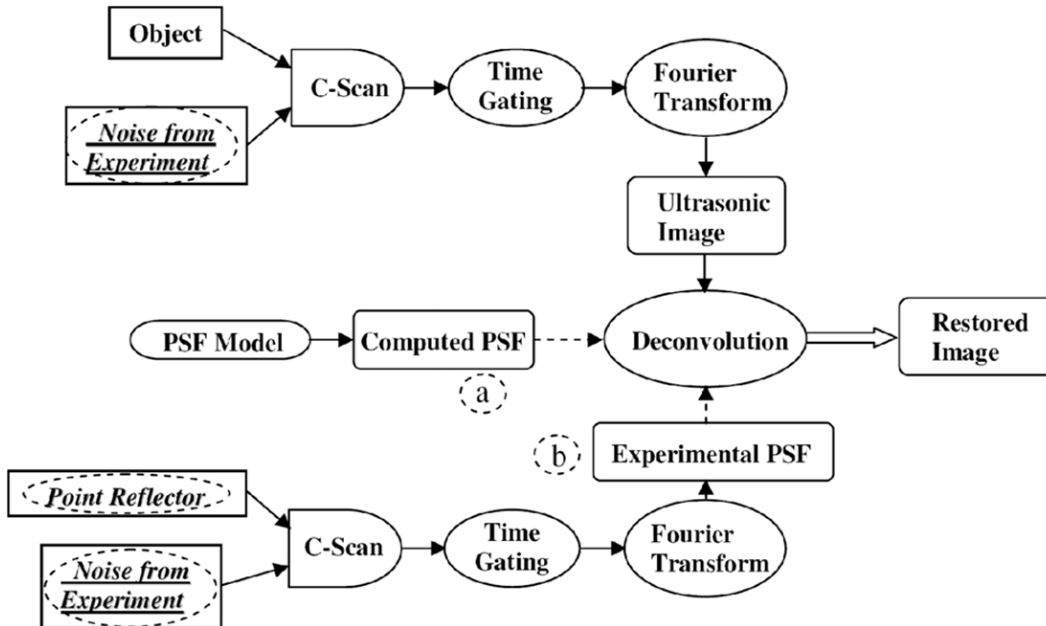Fig. 22. Flowchart outlining a procedure for characterization of planar transducers.

Fig. 23. Flowchart describing the PSF-based deconvolution using a characterized transducer. Option (a) is recommended; option (b) is for improved image restoration through deconvolution.

References

[1] R. S. Gilmore, "Industrial ultrasonic imaging and microscopy," *J. Phys. D: Appl. Phys.*, vol. 29, pp. 1389–1417, 1996.

[2] J. Zhao, P. A. Gaydecki, and F. M. Burdekin, "Investigation of block filtering and deconvolution for the improvement of lateral resolution and flaw sizing accuracy in ultrasonic testing," *Ultrasonics*, vol. 33, pp. 187–194, 1995.

[3] S. Wan, B. I. Raju, and M. A. Srinivasan, "Robust deconvolution of high-frequency images using higher-order spectral analysis and wavelets," *IEEE Trans. Ultrason., Ferroelect., Freq. Contr.*, vol. 50, no. 10, pp. 1286–1295, 2003.

[4] G. Dougherty and Z. Kawaf, "The point spread function revisited: Image restoration using 2D deconvolution," *Radiography*, vol. 7, pp. 255–262, 2001.

[5] S.-W. Cheng and M.-K. Chao, "Resolution improvement of ultrasonic C-scan images by deconvolution using the monostatic point-reflector spreading function (MPSF) of the transducer," *NDT&E Int.*, vol. 29, no. 5, pp. 293–300, 1996.

[6] J. J. Stamnes, *Waves in Focal Regions.* Bristol, UK: Hilger, 1986.

[7] J. J. Wen and M. A. Breazeale, "A diffraction beam field expressed as the superposition of Gaussian beams," *J. Acoust. Soc. Amer.*, vol. 83, pp. 1752–1756, 1988.

[8] L. W. Schmerr, *Fundamentals of Ultrasonic Nondestructive Evaluation: A Modeling Approach.* New York: Plenum Press, 1998.

[9] K. B. Ocheltree and L. A. Frizzell, "Sound field calculation for rectangular sources," *IEEE Trans. Ultrason., Ferroelect., Freq. Contr.*, vol. 36, no. 2, pp. 242–248, 1989.

[10] C. V. Krishnamurthy, M. Shankar, J. V. Vardhan, and K. Balasubramaniam, "The 2004 ultrasonic benchmark problem—SDH response under oblique incidence: Measurements and patch element model calculations," *Rev. Quant. Nondestr. Eval.*, vol. 25, pp. 1820–1827, 2005.

[11] L. M. Brekhovskikh, *Waves in Layered Media.* New York: Springer-Verlag, 1960.

[12] D. Reilly and G. Hayward, "A model to predict the transient radiation from segmented annular apertures radiating in to solid media," *IEEE Trans. Ultrason., Ferroelect., Freq. Contr.*, vol. 43, no. 2, pp. 263–269, 1996.

[13] J. Y. Lu and J. E. Greenleaf, "Ultrasonic nondiffracting transducer for medical imaging," *IEEE Trans. Ultrason., Ferroelect., Freq. Contr.*, vol. 37, pp. 438–447, 1990.

[14] M. Born and E. Wolf, *Principles of Optics.* 6th ed. New York: Pergamon Press, 1980.

C. V. Krishnamurthy was born in Chennai, India in 1960. He received the Master's degree in physics from the Indian Institute of Technology, Mumbai, India, in 1982, and the Ph.D. degree in condensed matter physics from the Indian Institute of Technology, Madras, India, in 1989.

He worked as a lecturer at the NCERT Regional College of Education, Mysore, India, during 1989–1990. During 1990–1993, he worked on a CSIR postdoctoral fellowship on third-order nonlinear optical susceptibilities in color center crystals at the Department of Physics, Indian Institute of Technology, Madras. From 1993 until 2002, he worked as a staff scientist at Helios Systems and Software, Chennai, India. Since 2002, he is with the Centre for Nondestructive Evaluation (CNDE), Department of Mechanical Engineering, Indian Institute of Technology, Madras, as Principal Project Officer.

Dr. Krishnamurthy's earlier work included developing computational methods and codes for assessing platform obscuration effects on antenna radiation patterns and atmospheric effects on radiowave and infrared propagation over the sea. His current work involves development of quantitative models and designing experimental schemes for utilizing ultrasound, eddy-current, microwaves, and infrared frequencies for flaw detection, imaging, and material characterization.

Krishnan Balasubramaniam has been involved in the field of sensors, acoustics, and nondestructive evaluation (NDE) for more than twenty years, with application of NDE technology in the fields of maintenance, quality assurance, manufacturing, and design. He is currently a professor in the Department of Mechanical Engineering and serves as the Head of the Centre for Nondestructive Evaluation at the Indian Institute of Technology, Madras. He graduated from the Department of Mechanical Engineering, Drexel University, Philadelphia, with a Ph.D. degree in 1989. He was an associate professor in the Department of Aerospace Engineering and Mechanics, Mississippi State University, Mississippi, MS, from 1991-2000. His areas of specialization include nondestructive evaluation, intelligent manufacturing and in-process monitoring, structural health monitoring, and applied data analysis. He currently serves on the Editorial Board of the Journal for Nondestructive Testing and Evaluation.
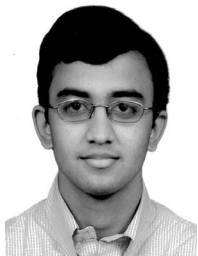
Ramsharan Rangarajan was born in Trichy, India, in 1984. He received a Bachelor's degree in mechanical engineering from the Indian Institute of Technology, Madras, India, in 2006. He is currently a graduate student in the Department of Mechanical Engineering at Stanford University, Stanford, CA.